Supplementary Information (SI) for Lab on a Chip.

Supplementary Information

A Portable Modular Acoustic Streaming Vortex Platform for Flexible and Robust Fabrication of Monodisperse Micromaterials

Xiaoping Miao,[a,b,c,†] Tianao Chen,[a,b,c,†] Jijie Fu,[d] Shilu Zhu,[a,b,c] Mei Lan,[a,b,c] Huayi Fu,[a,b,c] Zhiqiang Zhu,[d] Mingzhai Sun,[a,b,c] Ronald X Xu[a,b,c,*]

[a] School of Biomedical Engineering, Division of Life Sciences and Medicine, University of Science and Technology of China, Hefei, Anhui, 230026, P.R.China;

[b] Suzhou Institute for Advanced Research, University of Science and Technology of China, Suzhou, Jiangsu, 215123, P.R.China;

[c] Jiangsu Provincial Key Laboratory of Multimodal Digital Twin Technology, Suzhou, Jiangsu, 215123, P.R.China;

[d] Department of Precision Machinery and Precision Instrumentation, University of Science and Technology of China Hefei, Anhui 230026, P.R.China.

[†] These authors contributed equally to this work.

[*] E-mail: xux@ustc.edu.cn

This PDF file includes:
Supplementary Text
Figures S1 to S11.
Tables S1 to S2.
Movies S1 to S3.

Supplementary Text

Acoustic field simulation

Acoustic streaming induced by the sound field is a stable fluid flow generated by the nonlinear terms in the Navier-Stokes equations. From a mathematical perspective, the sound field represents the first-order linearized field of the Navier-Stokes equations, while the acoustic flow field describes the time-averaged second-order field of the system's disturbances. The classical method for calculating acoustic streaming patterns is perturbation theory. In the absence of external forces or thermal sources, for an isotropic, homogeneous, incompressible viscous fluid, the mass and momentum conservation equations governing the flow are as follows:

$$\nabla \cdot \nu = 0 \tag{1}$$

$$\frac{\partial \nu}{\partial t} + (\nu \cdot \nabla)\nu = -\frac{1}{\rho}\nabla p + \mu \nabla^2 \nu \tag{2}$$

where ν is the velocity vector of the fluid; p is the pressure; and μ is the dynamic viscosity of the fluid.

Using Nyborg's perturbation method, the flow process can be decomposed into the superposition of vibrational flow and steady flow. This simulation primarily investigates the steady flow induced by sound (periodic forcing), so the velocity and pressure fields can be decomposed as:

$$\nu = \nu_0 + \nu_1 + \nu_2 \tag{3a}$$

$$p = p_0 + p_1 + p_2 \tag{3b}$$

where ν_0 、ν_1 and $\nu_2$represent the undisturbed flow, the oscillatory (first-order small) component, and the time-averaged flow component (second-order small), respectively. Here ν_1=$v_a e^{-i\omega t}$ (where v_a is the amplitude of the vibrational velocity). Since the undisturbed flow is static (no mean directional flow), $\nu_0 = 0$.

p_0、p_1 and p_2 correspond to the reference pressure, oscillatory pressure (first-order small), and steady pressure (second-order small), respectively. The reference pressure is equal to atmospheric pressure, p_0 = patm.

Substituting equations (3) into (1) and (2), and extracting the first-order small terms, we obtain the following form:

$$\nabla \cdot v_1 = 0 \tag{4}$$

$$\frac{\partial v_1}{\partial t} + (v_1 \cdot \nabla)v_1 = -\frac{1}{\rho}\nabla p_1 + \mu\nabla^2 v_1 \tag{5}$$

Considering the small vibrational amplitude and $v_0 = 0$ in this study, the nonlinear term $(v_1 \cdot \nabla)v_1$ can be neglected, equation (5) can be simplified to the first-order equation:

$$i\omega v_1 = -\frac{1}{\rho}\nabla p_1 + \mu\nabla^2 v_1 \tag{6}$$

Substituting equation (3) into equations (1) and (2), extracting second-order small terms, and performing time-averaging, we arrive at the second-order small equation:

$$\nabla \cdot v_2 = 0 \tag{7}$$

$$(v_2 \cdot \nabla)v_2 + \langle (v_1 \cdot \nabla)v_1 \rangle = -\frac{1}{\rho}\nabla p_2 + \mu\nabla^2 v_2 \tag{8}$$

At this stage, $\rho\langle (v_1 \cdot \nabla)v_1 \rangle$ becomes the force term (F), in the steady-state Navier-Stokes equation, which can be expressed as:

$$F = -\frac{\rho}{2}\begin{pmatrix} v_{1x} \cdot \frac{\partial v_{1x}}{\partial x} + v_{1y} \cdot \frac{\partial v_{1x}}{\partial y} \\ v_{1x} \cdot \frac{\partial v_{1y}}{\partial x} + v_{1y} \cdot \frac{\partial v_{1y}}{\partial y} \end{pmatrix} \tag{9}$$

Based on these derived equations, we utilized COMSOL simulation software to model and simulate the acoustic droplet generator. The simulation domain consists of a 40 x 20 mm liquid domain near the sharp-edge structure of the microfluidic channel, and a capillary domain. The liquid domain properties were set based on the physical parameters of water, while the capillary domain properties were defined according to the attributes of the sharpened metal needle. The dimensions of the needle were defined based on its microscopic image, with the needle tip sharpness set to 0.6 mm, the outer diameter of the needle tip to 0.24 mm, and the inner diameter to 0.16 mm.

Forced oscillation regime of the capillary

The selected nozzle is composed of a nickel-plated brass needle hub welded to a stainless steel capillary. The outer diameter of the nozzle hub (D_1) is ~3.3 mm, while that of the capillary (D_2) is only 0.31 mm, with a capillary length (L) of 13 mm. The D_1/D_2 ratio exceeds 10, so the structure can be treated as a fixed-end cantilever beam. Meanwhile, the length-to-diameter ratio L/D_2 is ~42, far above 10. This meets the slender beam requirement of Euler-Bernoulli beam theory, confirming the capillary's outstanding flexibility. According to the following equation, this problem can be approximately described as motion with non-uniform mass distribution and damping effects. Therefore, the motion of the lower end of the nozzle is simple harmonic motion under steady-state conditions, whose amplitude and phase are significantly affected by the fluid action.

$$EI\frac{\partial^4 y}{\partial x^4} + \rho A\frac{\partial^2 y}{\partial t^2} = F_{fuid}(x,t) \tag{1}$$

$$F_{fuid}(x,t) = - m\frac{\partial^2 y}{\partial t^2} - C\frac{\partial y}{\partial t} \tag{2}$$

Where, L is the rod length, EI is the flexural rigidity, and ρA is the linear density.

The right-hand side of the equation represents the distributed force exerted by the fluid on the rod, which exists only in the portion submerged in water.

The added mass force $m\frac{\partial^2 y}{\partial t^2}$: reflects the inertial effect of water being driven by the rod to move together, equivalent to increasing the effective mass of the rod.

The damping force $C\frac{\partial y}{\partial t}$: caused by the viscosity of water and wave radiation, dissipates vibrational energy and attenuates the amplitude. It is proportional to the vibration velocity of the rod and reflects the energy exchange between the rod and the fluid: part is dissipated as heat, and the other part is converted into the kinetic energy of the fluid, driving the fluid to form vortices.

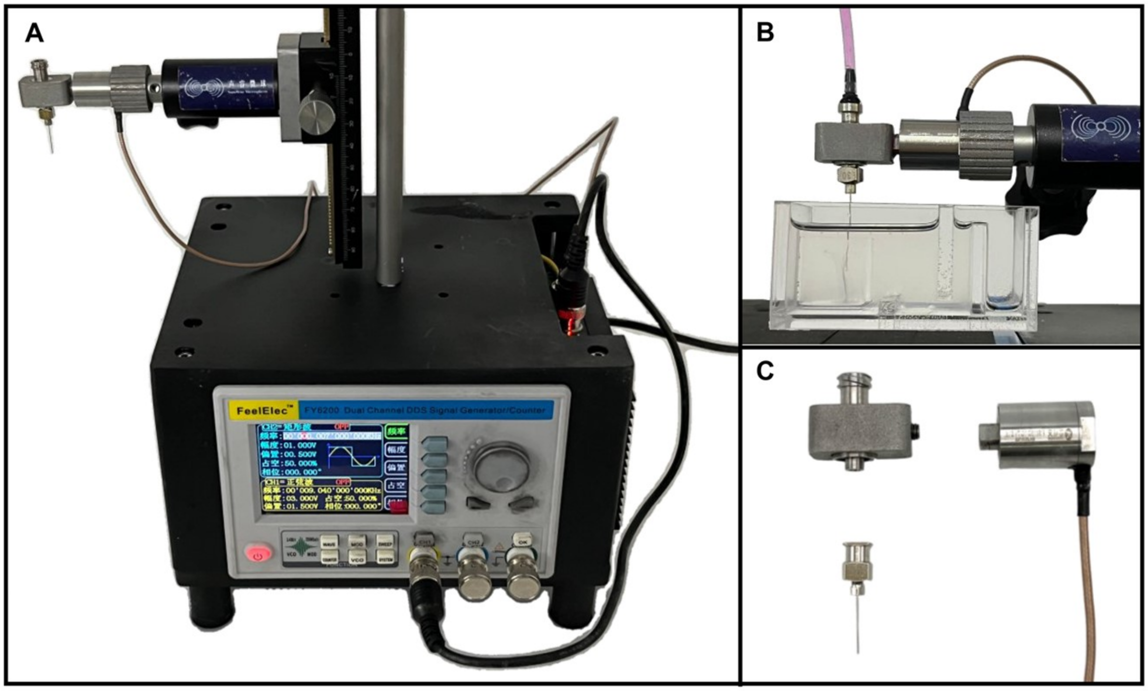

Figure S1. (A) Schematic of the overall structure of the MVSA platform. (B) Photograph of the portable droplet generation platform based on acoustic streaming vortex effects during microdroplet generation. (C) Exploded view and assembled diagram of MVSA components.

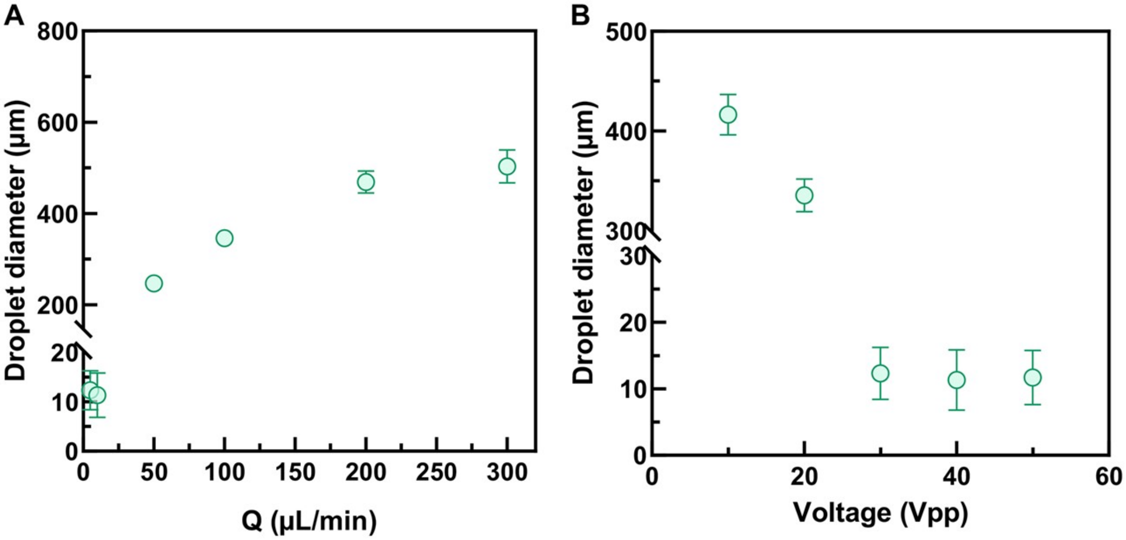

Figure S2. Atomization regime of water-oil system microdroplets. (A) Effect of dispersed phase flow rate on droplet size range and variation trends. (B) Effect of input voltage on droplet size range and variation trend.

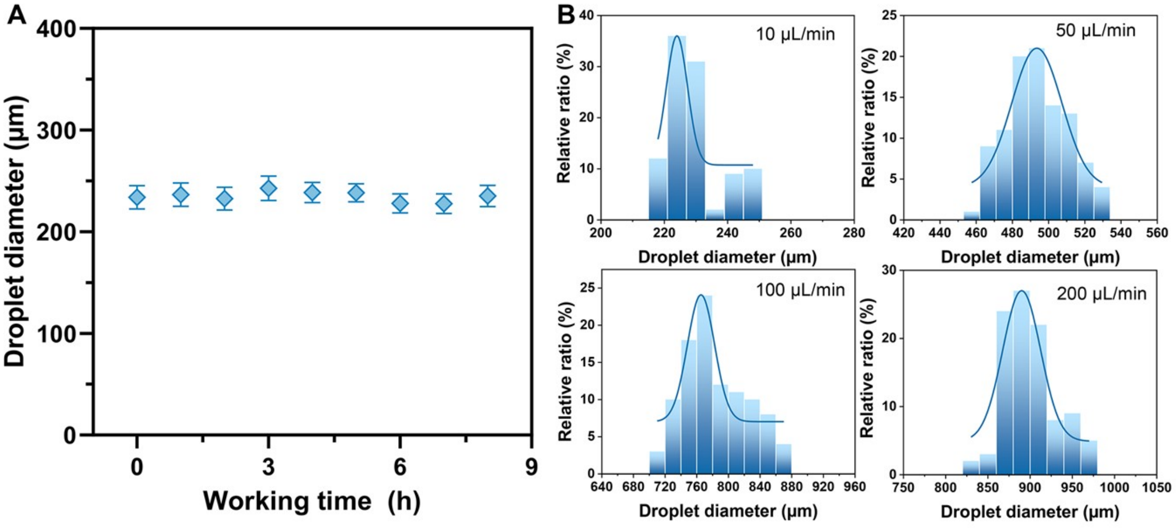

Figure S3. (A) Droplet size variation during continuous operation of the device under dripping regime. (B) Droplet size distribution histogram at different flow rates under dripping regime.

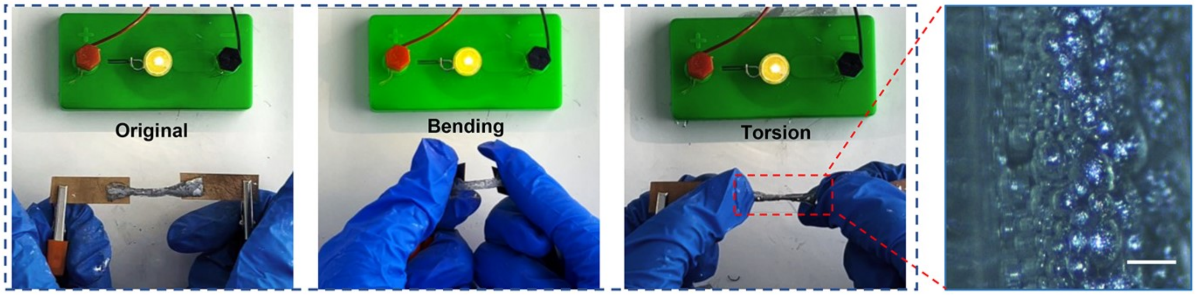

Figure S4. LM microdroplet-based hydrogel used to illuminate a small light bulb (left). Cross-sectional views of LM hydrogels (Right). Scale bar: 200 μm.

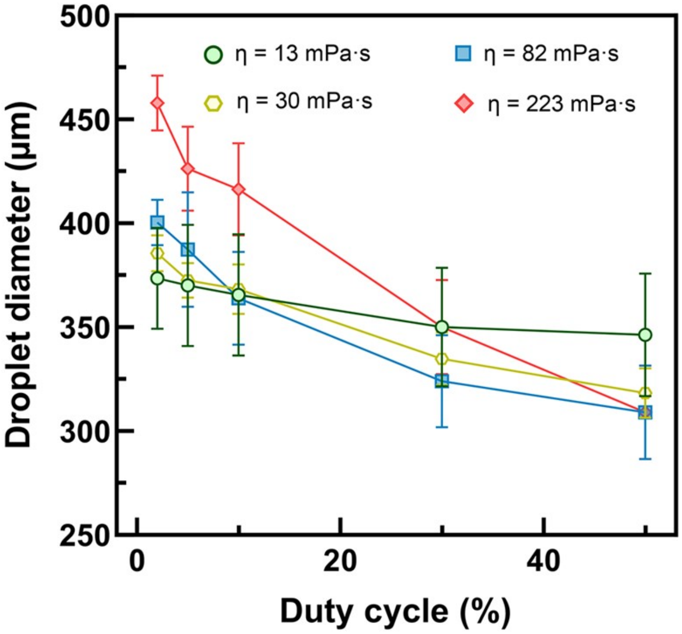

Figure S5. Under AM mode, the relationship between droplet size and variations in duty cycle for glycerol solutions of different viscosities.

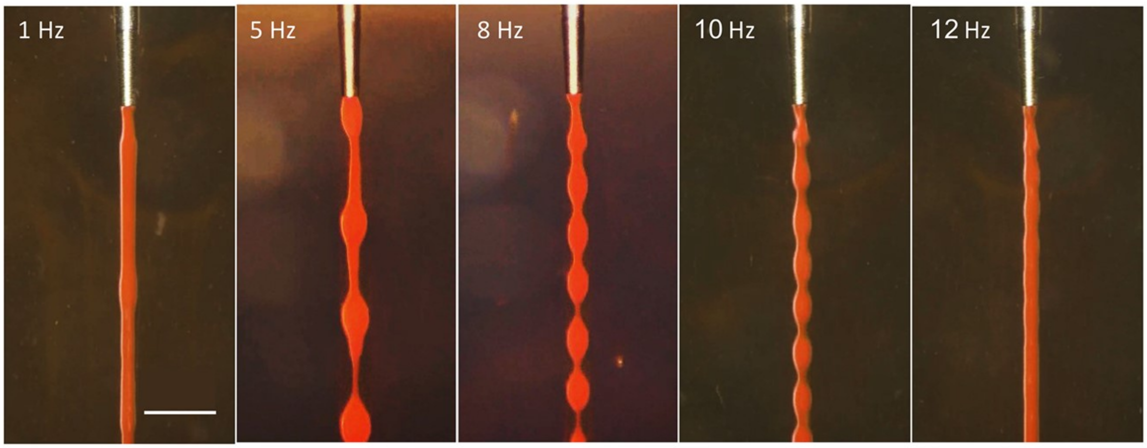

Figure S6. Optical micrographs of knotted microfibers at different AM frequencies. Scale bar: 1 mm.

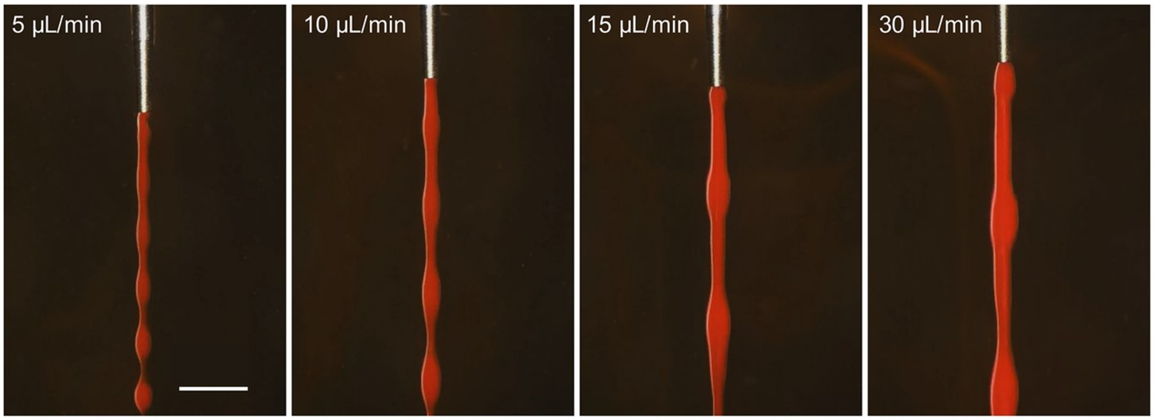

Figure S7. Optical micrographs of knotted microfibers at different pumping flow rates. Scale bar: 1 mm.

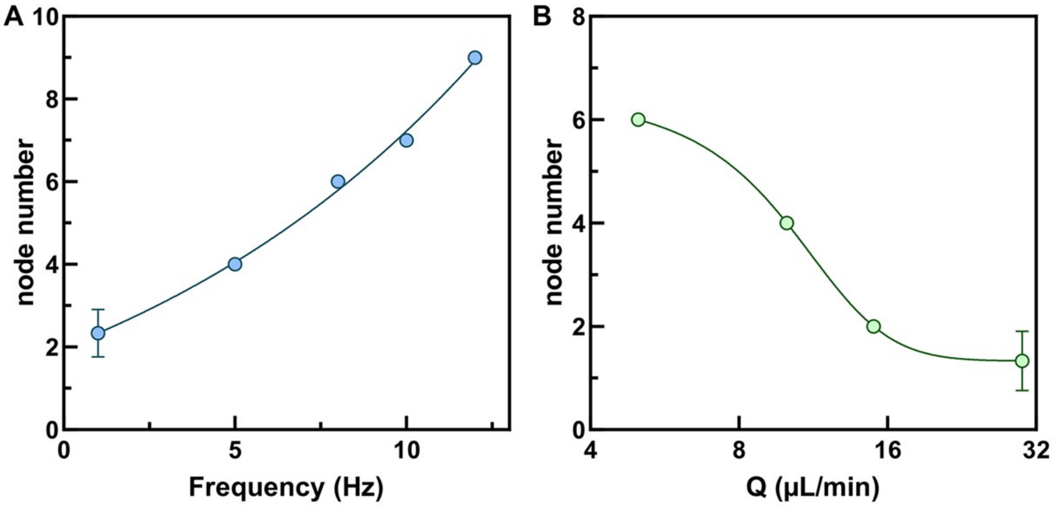

Figure S8. Relationship between the number of knots per unit length and changes in AM frequency (A) and injection flow rate (B).

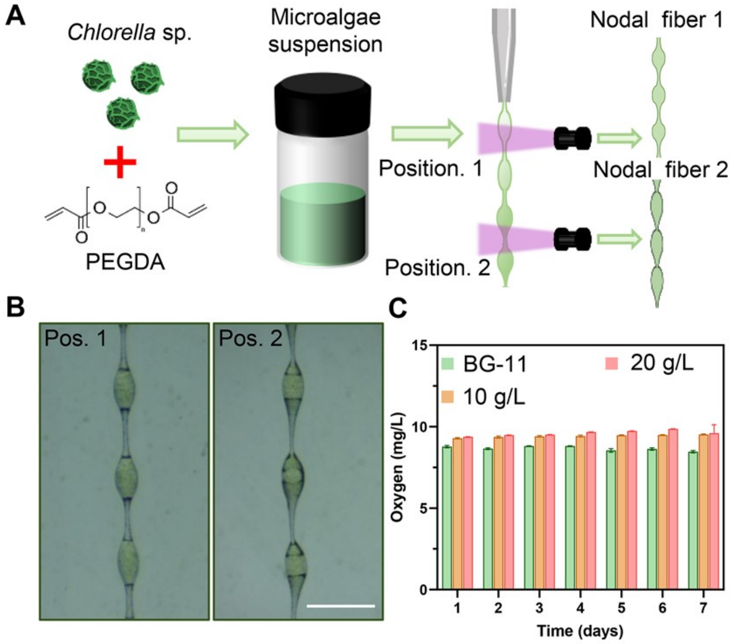

Figure S9. (A) Schematic of cyanobacteria fiber preparation. (B) Optical microscopy images of cyanobacteria-loaded fibers with distinct morphologies at different positions. Scale bar: 1 mm. (C) Oxygen release profile of cyanobacteria fibers at various concentrations after seven days.

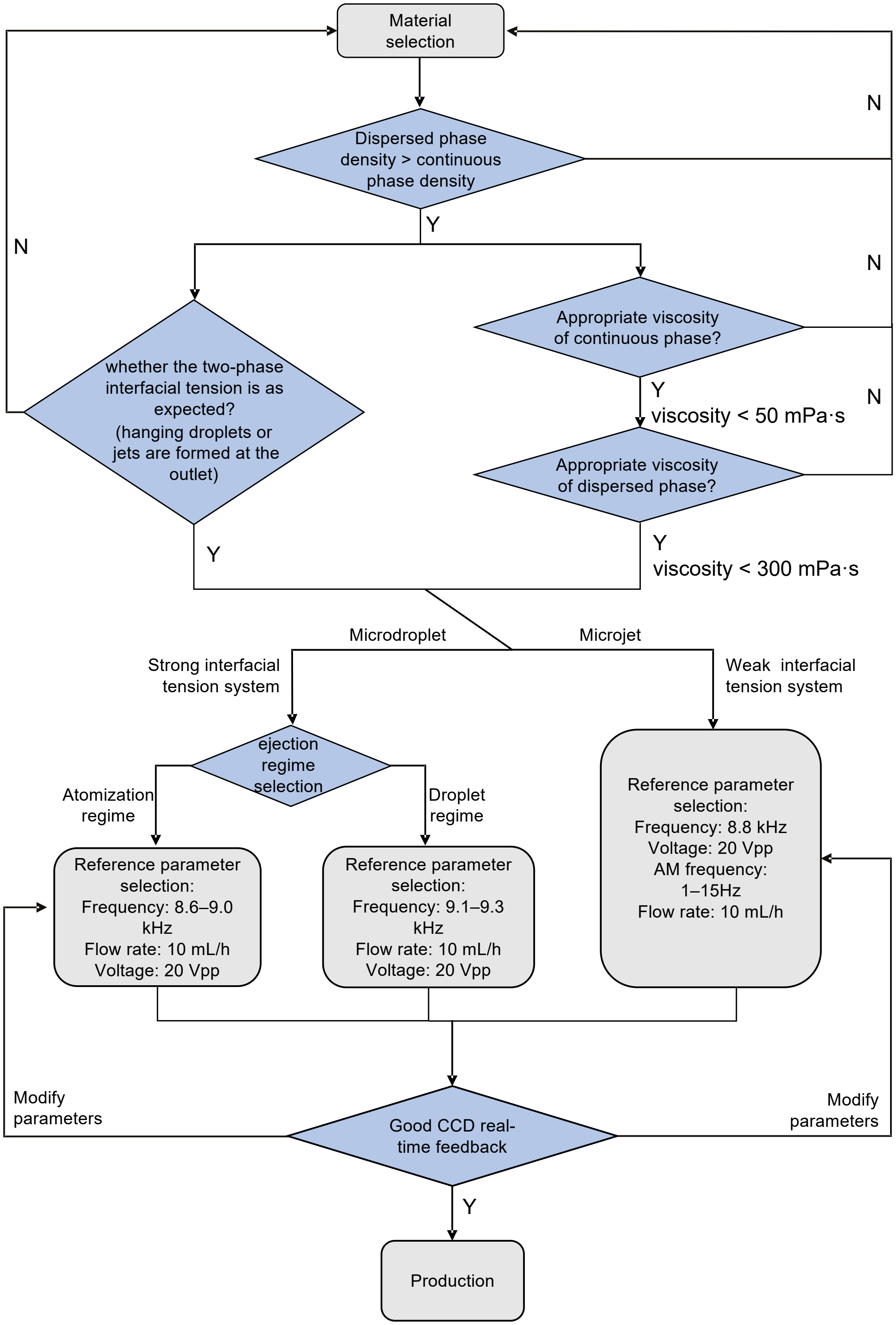

Figure S10. Operating flowchart for experimental parameter selection.

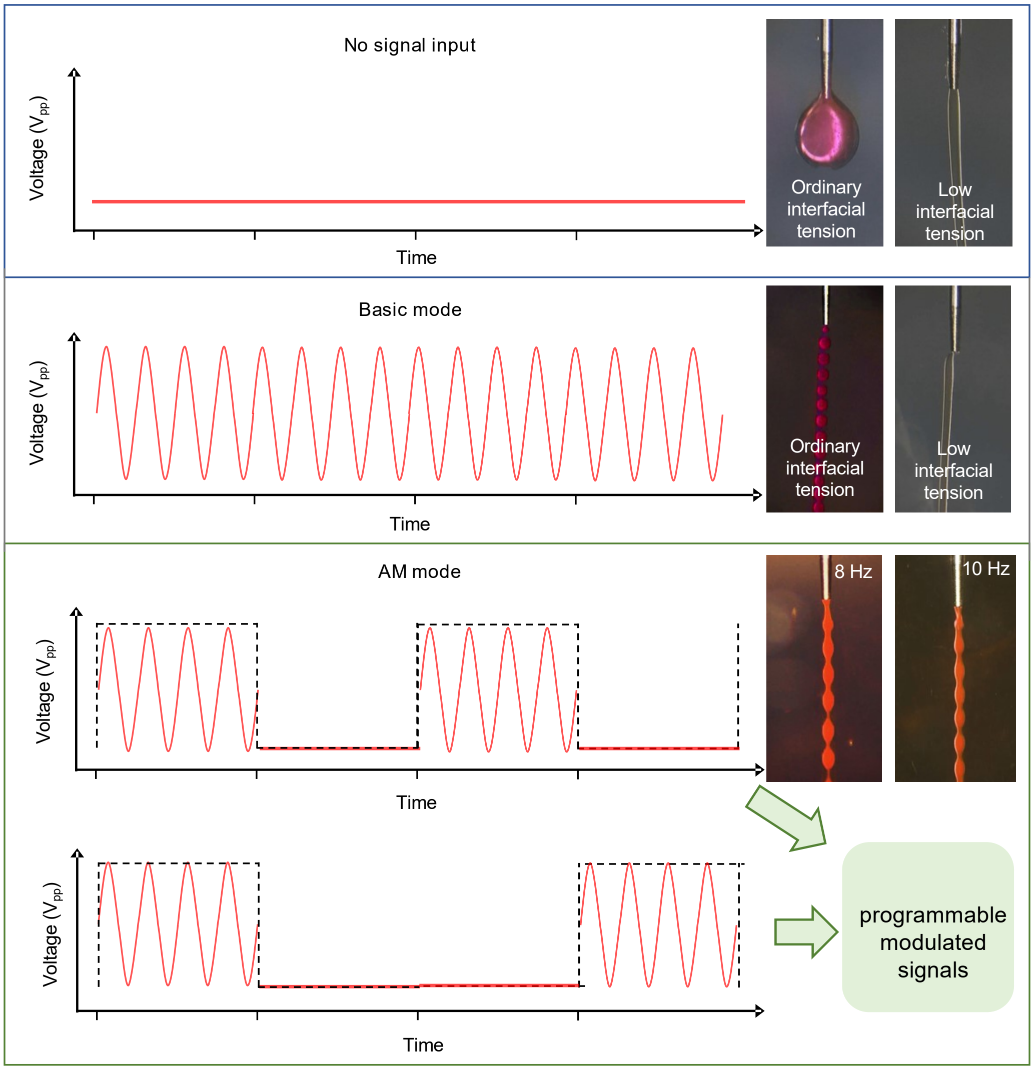

Figure S11. Comparison of different input signals.

Table S1. Comparisons of different microfluidic techniques for the production of normal droplets

Droplet generation method	Droplet generation principle	Droplet size range	Size tuning flexibility	Fluids selection range	Morphological diversity	Device System complexity	Ref.
On-chip microfluidics	Hydrodynamic pressure of the flow (coflow, T-junction and flow-focusing)	10 µm ~ 1 mm (determined by chip channel dimensions)	Moderate	Moderate	Multimorphology microdroplets	High	[1, 2]
In-air microfluidics	In-air impact, encapsulation, and solidification	20-300 µm (vary nozzle)	Low	Narrow	Microdroplets; Microfibers	High	[3]
Electrospray	Imbalance between the electrostatic force and surface tension	5-150 µm (fixed nozzle)	Moderate	Moderate	Microdroplets	Low	[4]
Inkjet printing	Pressure pulses generated in the fluid	50-110 µm (fixed nozzle)	Low	Narrow	Microdroplets; Microfibers	High	[5]
Programmable pulsed aerodynamic printing	Shearing suspended droplets with pulsed high-speed airflow	100-700 µm (fixed nozzle)	Moderate	Wide	Microdroplets	High	[6]
Vertical step emulsification	Interfacial tension difference when dispersed phase flows out of the gap	150-300 µm (fixed nozzle)	Low	Moderate	Microdroplets	Low	[7]
Wetting-induced interfacial instability	Wetting-induced interfacial instability for droplet emission at air-liquid interfaces	40-470 µm (fixed nozzle)	Moderate	Wide	Microdroplets	Low	[8]
Modular acoustic vortex microfluidic	**Vibrating effect and acoustic streaming vortex shearing**	**13-750 µm (fixed nozzle)**	**High**	**Wide**	**Microdroplets; Microfibers**	**Low**	

Table S2. Nozzle size parameters

Nozzle Specification code	Inner Diameter (mm)	Front Outer Diameter (mm)	Syringe Outer Diameter (mm)
28G	0.18	0.27	0.35
30G	0.16	0.24	0.31
32G	0.10	0.18	0.25
34G	0.06	0.12	0.25

Vedio S1.

Regulation of Droplet or Fiber Generation from Different Inks.

Vedio S2.

Real-Time Tuning of Droplet Sizes via Simple Frequency Adjustment of the Output PD frequency.

Vedio S3.

Real-Time Visualization of the Liquid Metal Formation Process.

References

1. M. I. Hajam, M. M. Khan, “Microfluidics: a concise review of the history, principles, design, applications, and future outlook,” Biomaterials Science 12, no. 2 (2024): 218-251.
2. K. O. Rojek, M. Cwiklinska, J. Kuczak, et al., “Microfluidic formulation of topological hydrogels for microtissue engineering,” Chemical Reviews 122, no. 22 (2022): 16839-16909.
3. C. W. Visser, T. Kamperman, L. P. Karbaat, et al., “In-air microfluidics enables rapid fabrication of emulsions, suspensions, and 3D modular (bio) materials,” Science advances 4, no. 1 (2018): eaao1175.
4. Z. Pan, Y. Men, S. Senapati, et al., “Immersed AC electrospray (iACE) for monodispersed aqueous droplet generation,” Biomicrofluidics 12, no. 4 (2018).
5. W. Zhang, N. Li, D. Koga, et al., “Inkjet printing based droplet generation for integrated online digital polymerase chain reaction,” Analytical chemistry 90, no. 8 (2018): 5329-5334.
6. Z. Zhu, T. Chen, Y. Zhu, et al., “Programmable pulsed aerodynamic printing for multi-interface composite manufacturing,” MATTER 6, no. 6 (2023): 2034-2051. DOI 10.1016/j.matt.2023.04.017.
7. Y. H. Hwang, J. H. Lee, T. Um, et al., “3D printing of monolithic gravity-assisted step-emulsification device for scalable production of high viscosity emulsion droplets,” Lab on a Chip 24, no. 20 (2024): 4778-4785.
8. Y. Y. Su, D. W. Pan, T. X. Zhang, et al., “Wetting-induced interfacial instability: A mechanism for droplet emission at air-liquid interfaces,” Science Advances 11, no. 12 (2025).